http://dx.doi.org/10.1016/j.ijmachtools.2021.103713

Modelling of ultra-thin steel sheet in two-stage tensile deformation considering strain path change and grain size effect and application in multi-stage microforming

Abstract

Multi-stage plastic deformation of metallic sheets for fabrication of complex micro structures with high aspect ratio features in different industrial clusters has been prevailing due to product miniaturization and integrated manufacturing. Owning to the varying strain path and the miniaturized scale of work pieces, both the strain path change (SPC) and size effect (SE) significantly affect the behaviors and phenomena in micro-scaled deformation. The influence of SPC loading on micro-scaled deformation and its mechanism have not yet been systematically investigated and an in-depth knowledge of the microstructure evolution at grain-level affected by the SE also needs to be explored under different deformation conditions. To have a scientific insight and understanding of the interaction between SPC and SE, two-stage tensile tests were conducted using the 0.1 mm thick SS 316L sheets with different grain sizes. High resolution microscopy was employed to characterize the microstructure evolutions under the varying strain path loading. A micro-scale mechanism-based constitutive model considering both the SPC and SE was established for predicting the flow stress in multi-stage deformation of ultra-thin sheets. The results showed that the yield stress and elongation rate in the second loading stage were decreased with the increase of pre-strain and the intersection angle between two loading directions; while the hardening rate was found to be solely dependent on pre-strain. The orientation preference after the first stage tension was reversed by changing the loading direction in the second stage, which raises the percentage of high Schmid factor and thus lowers the yield stress and hardening rate. On the other hand, the coarsened grains attain more inner mismatching boundaries in the first stage deformation, which impedes the dislocation movement and increases the flow stress. These two confronted mechanisms of SPC and SE interactively influence the deformation behaviors. The

high Schmid factor percentage was found to be associated with the defined SPC parameter in a quadratic manner and this relationship was employed in the development of constitutive model for describing the flow stress affected by SPC and SE. An in-depth understanding of the interactive effects of SPC and SE on deformation behaviors and micro-scale mechanisms of ultra-thin 316L sheets was thus established for providing a basis to support multi-stage forming of complex micro-scaled parts.

Keywords

Ultra-thin sheets; multi-stage deformation; micro-scaled deformation; strain path change; size effect.

1. Introduction

Miniaturized metallic parts and structures have been widely used in various industrial clusters and micro sheet forming has been proven to be an efficient and low cost technology for mass production of metallic micro parts and structures [1]. Due to the growing demand for quality products, manufacturing of complex parts and structures with high precision and accuracy using ultra-thin metallic sheets has become a challenging issue for micro forming of sheet metals [2]. Micro channel with fine width and high aspect ratio is the kernel feature of the ultra-thin metallic bipolar plates (BPP) in proton exchange membrane fuel cell (PEMFC) [3]. Generally, the metallic sheets can be easily fractured in conventional one-stage forming, especially when fabricating micro features with concentrated thickness reduction and large deformation [4, 5]. To address this issue, multi-stage forming is adopted to reasonably distribute deformation into different forming stages and accommodate a more uniform deformation, so local thickness reduction can be reduced and good geometry accuracy can be obtained by using tailor designed tools stage by stage [6, 7]. For multi-stage forming, uniformly distributed thickness and accurate profile are based on the

optimization of forming parameters [8], which can be conducted by FEA simulation with high efficiency and low cost [9]. In this case, a precise constitutive model predicting the flow stress of ultra-thin sheets in multi-stage forming is of great significance. Since the loading path varies in each forming stage, the strain path correspondingly changes and consequently influences the subsequent deformation responses [10]. In tandem with that, size effect (SE) also affects material's mechanical properties in micro forming [11]. Therefore, the two issues and their interaction need to be investigated in detail for an in-depth understanding and precise modeling of the multi-stage forming process.

Nonlinear strain path and varying strain state [12] can be commonly found in multi-pass [13] or multi-stage forming [14]. The influences of the varying deformation on material mechanical response have been especially studied in the fields of strain path change (SPC) [15]. There are two types of experimental methods classified based on whether the strain path is absolutely reversed: cyclic deformation and multi-stage deformation. For the first one, cyclic tension-compression [16], cyclic shearing/torsion [17] and bending [18] are generally used to study the Bauschinger effect [19]. For the other one, specimens are pre-strained in the first stage and then followed by other deformations with changing strain path [20]. Multi-stage tensile tests [21] are widely adopted for investigating the SPC effect, in which specimens with relatively large dimensions are stretched for a certain strain and small specimens are then cut out from the stretched large specimens along different directions. The change of strain path can be realized by the second stage tension with the pre-strained small specimens [15]. Experimental results revealed that the deformation induced anisotropy strongly influences the subsequent yielding loci [22], the forming limit [23, 24] and the flow stress characteristics such as the hardening/softening [25, 26] and varying hardening rate [27]. The multi-stage tension of pure aluminum and aluminum alloy sheets was conducted by Qin et al. [27] who found that the overshoot of the yield stress in the second tensile stage got increased with the intersection angle

between the two loading directions. According to the experiments done by Wen et al. [28] using magnesium alloy sheets, the yield stress in the second stage tension became smaller compared to the flow stress in monotonic tension with the same plastic strain and the deviations were increased with the intersection angle. Similar results were obtained by He et al. [29] using the thicker magnesium alloy sheets and the permanent softening in the second tensile stage was observed. In addition, the double phase steel sheets were used by Ha et al. [10] and Zaman et al. [30] for two-stage tension. It was found that the yield stress in the second tension had only a slight decrease and the stress-strain curves gradually got converged to those obtained in monotonic tension. Clarifying the multi-stage deformation behaviors especially for ultra-thin sheets is the research basis.

Conventional modeling and analysis methodologies developed for macro-scale manufacturing may not be fully valid and accurate when they are leveraged to micro-scale manufacturing for the existence of size effect [31, 32]. In micro sheet forming, size effect significantly influences the mechanical behaviors. Mahabunphachai and Koç studied the grain/specimen and feature/specimen size effect using hydraulic bulge tests with SS 304 sheets and verified that the flow stress was strongly dependent on these two ratios [33]. Based on the uniaxial tensile tests on pure copper foils with different thicknesses and grain sizes, Fu and Chan found that the fracture strain was decreased with the specimen/grain size ratio due to fewer activated slip systems [34]. Xu et al. systematically investigated the springback behaviors in pure copper sheets and found that the springback is gradually suppressed by reducing the ratio between the specimen thickness and grain size [35]. As discussed by Meyersm and Ashworth [36], the dislocations propagate inside the material and gradually move outside the material's free surface, during which the grain boundaries serve as the dislocation moving hinder. Therefore, the less boundaries the lower flow stress. In that case, decreasing the specimen dimensions or increasing the grain sizes both contribute to reducing grain boundaries and decreasing deformation resistance

[11], which just shows the interactive effects between the two types of SEs viz. the geometry and the grain size effects [37]. To individually study them, the first SE can be explored by keeping the grain size constant, while varying the feature/specimen size. The grain size effect, however, can be examined by keeping the feature/specimen size constant, but changing the grain size [38]. Among the models describing the influences of SE on the flow stress, the surface layer model [39] is widely adopted in micro forming [40]. It is assumed that the surface grains have less constraints than the inner ones and are easy to be deformed [41]. So once the volume fraction of surface grains is increased, the overall flow stress is correspondingly decreased [42].

For the multi-stage forming of ultra-thin metallic sheets, both the SPC and SE strongly influence the material deformation behaviors. Only a few grains accommodate the main deformation especially for the regions with micro features [43], so the local grain orientation and heterogeneity significantly affect the inhomogeneous deformation behavior in SPC micro forming. Nevertheless, few related researches have been conducted in the available reports and an in-depth understanding of the deformation mechanism at grain level is still insufficient. Although several phenomenon-based models [44] describing the SPC deformation behaviors have been reported, they are challenged in the robustness [27], efficiency [45] and experimental cost [46]. Besides, their applicability in micro forming is also limited because the neglect of size effect. It is crucial to elucidate the microstructure evolution influenced by SPC and SE for the insight into deformation's physical essence and establishing constitutive model with better flexibility and efficiency in micro-scale forming.

To address these issues, twofold attempts were made in this study. i) The mechanical responses of ultra-thin sheets with different grain sizes under SPC loading were investigated by two-stage tensile experiments and the influences of SPC and SE on the micro-scale deformation mechanism was unveiled based on the micro characterization. ii) A physical-based hybrid constitutive model considering both

influences of SPC and SE was developed and validated in the two-stage micro channel forming, so the flow stress of ultra-thin metallic sheets with different grain size in multi-stage micro forming can be predicted.

2. Experimental methodology and results

2.1 Material preparation and experiment design

Commercial austenite SS 316L metallic sheet with the thickness of 100.0 μm was used in this study. The as-received and after-heat-treatment (kept in 1050℃ for 3 hours) sheet specimens were prepared for experiment, so two types of specimens with fine grain (FG) size of 21.5±0.5 μm and coarse grain (CG) size of 74.6±0.5 μm were obtained. To get the mechanical properties of materials, uniaxial tensile tests were conducted by using the specimens designed following the ASTM-E8 standard with the testing machine, INSTRON5966 at a speed of 1.0 $mm \cdot min^{-1}$. The material chemical compositions are listed in Table 1 and the mechanical properties obtained from the true stress-strain curves shown in Fig. 1 are presented in Table 2.

Table 1 Chemical compositions of the commercial SS 316L.

Element	Fe	Cr	Ni	Mo	C	Mn	Co	Cu	V
Content/%	66.79	18.06	9.57	2.08	2.77	0.27	0.22	0.15	0.09

Table 2 Mechanical properties of the specimens. (Curves of rolling direction are fitted by Swift hardening $\sigma=K\left(\varepsilon_0+\varepsilon_p\right)^n$)

Specimen	Elastic modulus (GPa)	Yield stress (MPa)	K (MPa)	ε_0	n
Fine grain	225.6	260.5	1810.2	0.0746	0.747
Coarse grain	164.7	196.5	1398.1	0.0493	0.668

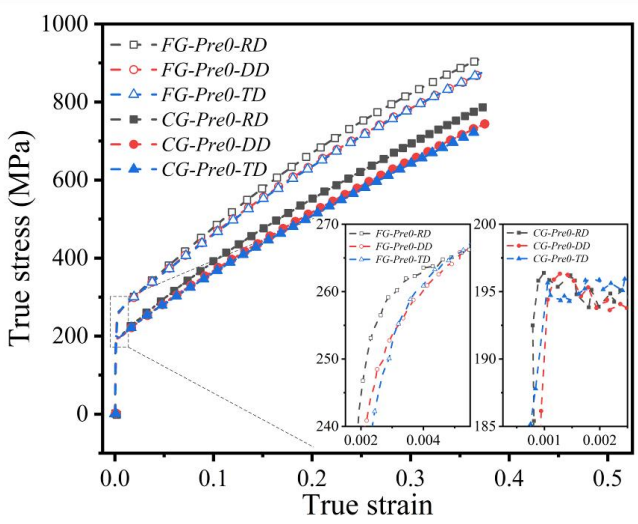

Fig. 1. True stress-strain curves of the uniaxial tensile tests along rolling direction (RD), diagonal direction (DD) and transverse direction (TD). "Pre0" indicates that the tension starts without pre-strain.

The diffraction density peaks identified by X-ray diffraction (XRD) and the metallography captured by optical microscopy (OM) are presented in Figs. 2 and 3. The standard powder diffraction file (PDF) data of austenite iron is also presented for comparison. The peak distributions are quite similar with the austenite data regardless of different grain sizes or pre-strains, indicating that the initial FCC matrix of the material is not changed by heat treatment or deformation.

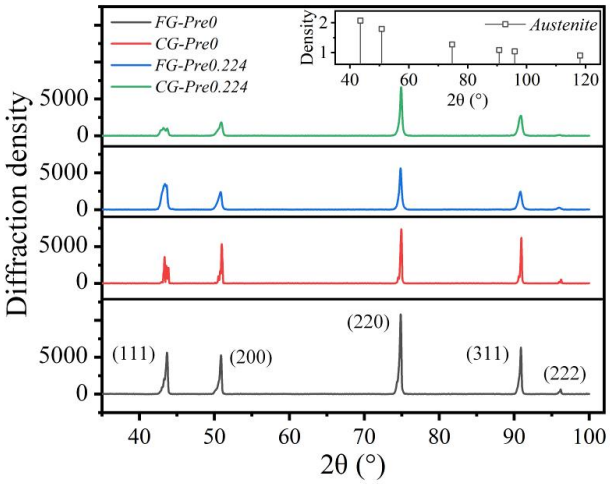

Fig. 2. Diffraction density distribution of the specimens under different conditions.

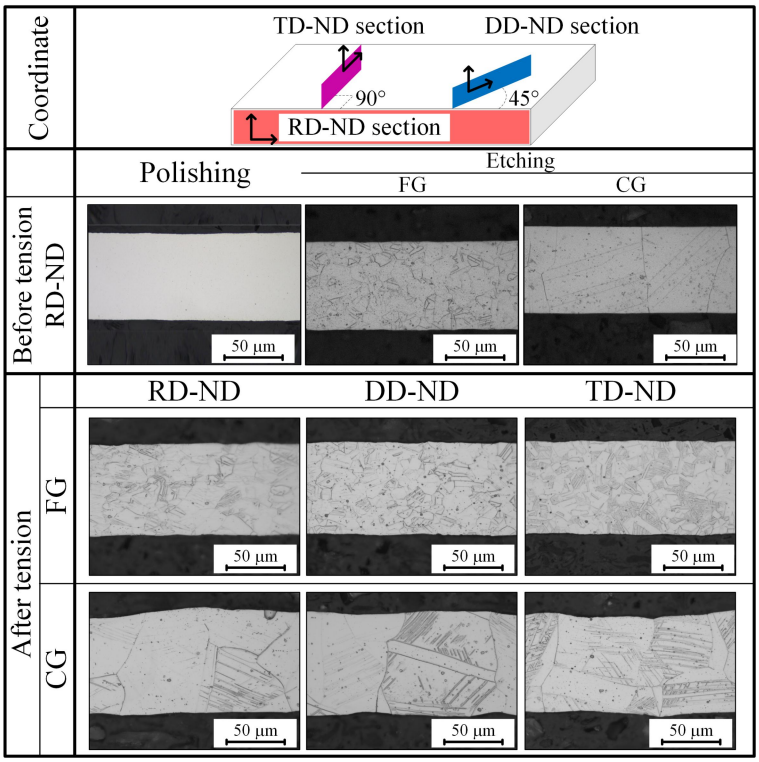

Fig. 3. Metallography of the specimens before and after deformation.

Two-stage tensile tests were designed for SPC deformation as shown in Fig. 4. The big size specimens were first stretched along the rolling direction (RD) to a certain strain; while the small size specimens were then cut along three directions, viz. RD, diagonal direction (DD) and transverse direction (TD) from the previously deformed big size specimens. The smaller specimens were stretched in the second stage. Different experiment conditions are determined by three parameters, viz. grain size, pre-strain and the direction of the second stage tension. The parameter design is given in Table 3. During the tensile procedures, GOM Aramis 4 M optical strain measurement system was used to measure the strain with a recording rate of five frames per second. A white and black random pattern was painted on the specimen surfaces before the tests, the strain could thus be measured by the digital image correlation (DIC) technique. For each case, at least three tests were repeated and the average stress-strain curves were adopted in this study.

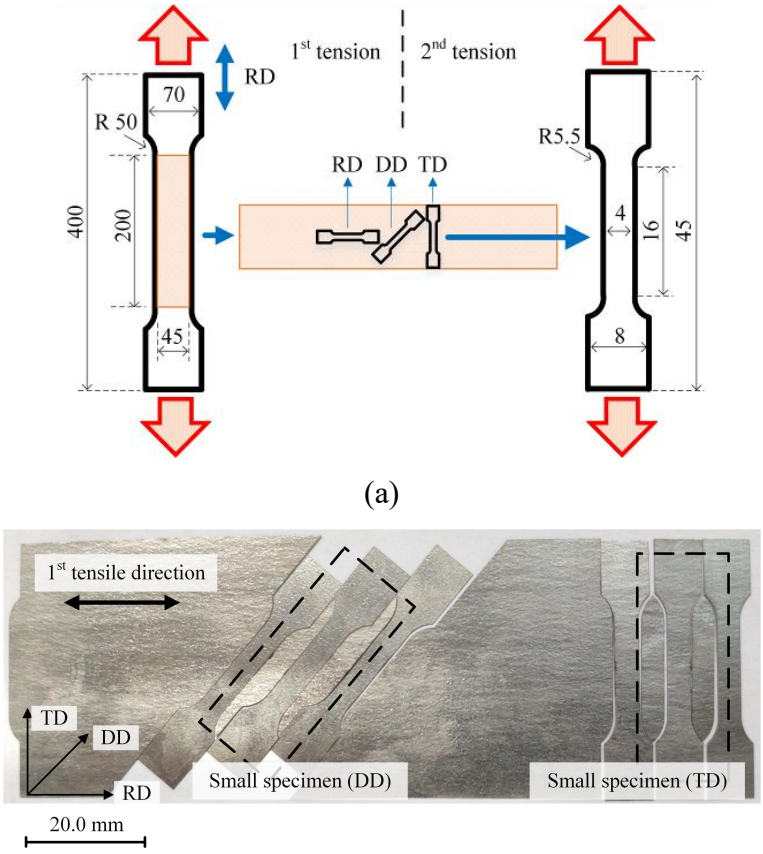

Fig. 4. Design of the two-stage tensile tests. a) schematic of the two-stage tensile test and the specimen dimensions; b) cutting of the DD and TD small size specimens.

Table 3 Design of the monotonic and two-stage tensile experiments

Parameters	First stage	Second stage
Grain size (μm)	21.5±0.5 & 74.6±0.5	21.5±0.5 & 74.6±0.5
Pre-strain	0	0.112 & 0.224
Final strain	0.112 & 0.224	0.1 & till break
Direction	RD	RD, DD, TD

2.2 Tensile test results

Two-stage tensile tests were performed using the parameters presented in Table 3. The true stress-strain curves of the monotonic and two-stage tension are plotted as Fig.

5 in which the second stage tensile curves start with the corresponding pre-strain. The yield stress and hardening rate are decreased when the strain path is changed. In addition, the decrease of the yield stress and hardening rate can be enlarged by increasing pre-strain and the intersection angle between the two loading directions. Similar tendency is observed in CG specimens but the difference is smaller. Based on the comparison between the monotonic and two-stage tensile curves, it is validated that the pre-strain, loading direction and grain size strongly influence the mechanical responses of the ultra-thin sheets in multi-stage deformation.

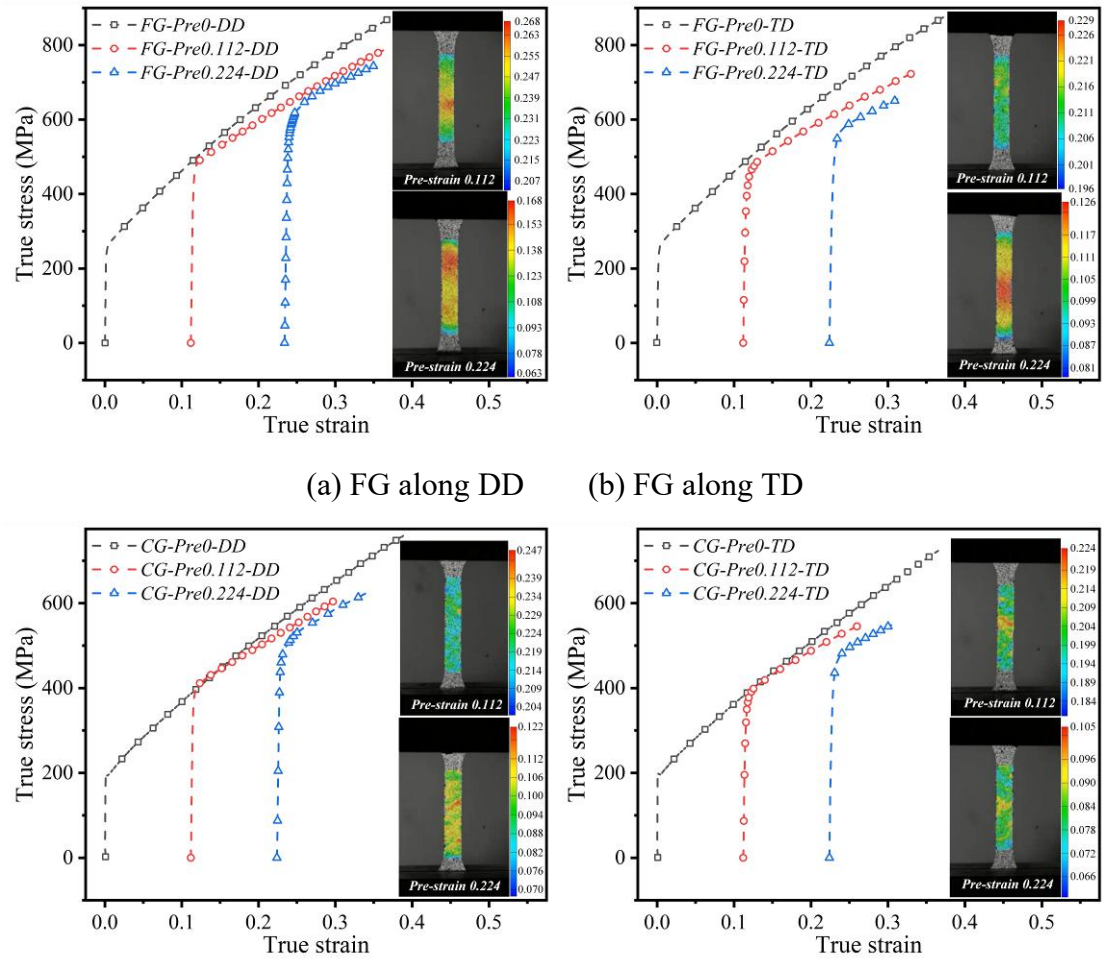

(a) FG along DD (b) FG along TD

(c) CG along DD (d) CG along TD

Fig. 5. True stress-strain curves of two-stage tensile tests. a) FG specimens stretched along DD in the second stage tension with pre-strain of 0.112 and 0.224 respectively; (b), (c), (d) present the results of the other cases.

In the case with the pre-strain of 0.112, the yield stress of the second stage is slightly lower than the flow stress of monotonic tension at the same strain but their difference is magnified when the pre-strain is increased to 0.224. The deviations are extracted and plotted in Fig. 6 and it is found that changing loading direction contributes to enlarging the deviations. When the tensile direction is fixed along DD, the yield stress deviations at the pre-strain of 0.112 and 0.224 are about 24 and 109 MPa respectively. However, when the tensile direction is changed to TD, the deviations are increased to 47 and 145 MPa. In addition, the deviation is much more significant in FG specimens indicating that coarsening grain size contributes to weakening the influences induced by increasing the pre-strain or changing the loading direction.

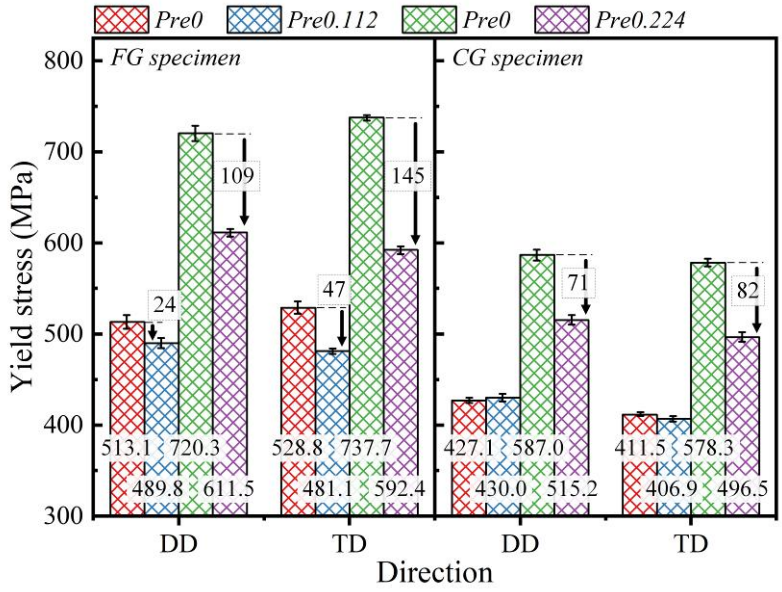

Fig. 6. The yield stress of the monotonic and two-stage tension at the same strain.

Evolution of the hardening rate is plotted in Fig. 7. Different from the effect in yield stress, the change of loading direction rarely influences the hardening rate which remains almost the same even though the tensile direction is changed from DD to TD. However, the hardening rate is decreased with the increase of pre-strain, e.g., it decreased about 200 MPa when the pre-strain is increased from 0.112 to 0.224 for FG

specimens. Similar tendencies can be observed in CG specimens which hardening rate is globally smaller than the results of FG specimens.

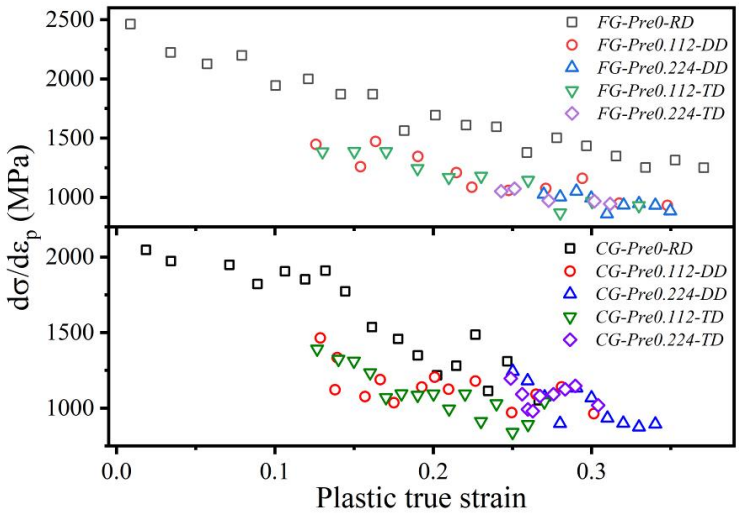

Fig. 7. The hardening rate evolution in each deformation condition.

The elongation rates ξ of specimens subjected to different deformation conditions are plotted in Fig. 8. FG specimens attain better elongation properties than the CG specimens, because the grain boundary constraint is weakened and the possibility of soft grains bearing the deformation is accordingly increased [1, 47]. It's found that ξ decreases with the increase of ε_{pre} and θ, which is attributed to the evolution of micro damage. In the first stage tension, micro voids nucleate and grow with the increase of strain [42]. In the second stage tension, the defect growth is enhanced when the loading direction is changed due to the stress concentration near the crack tips [48].

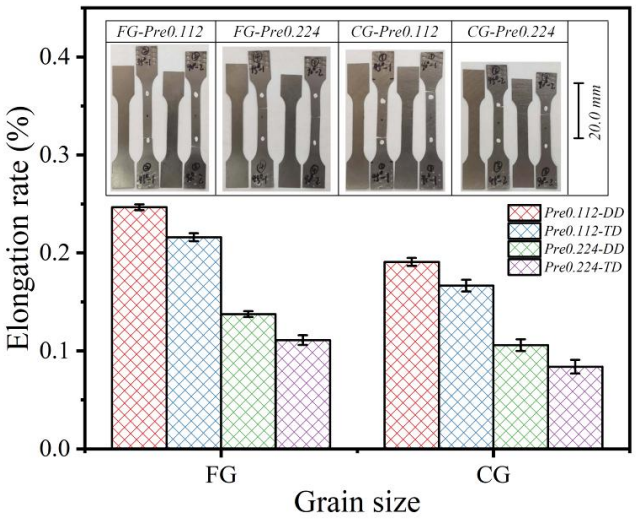

Fig. 8. The elongation rate of the specimens in the second stage tensile tests.

Influences of the grain size and strain path change on the macro-scaled mechanical properties are summarized in Table 4. Compared to the monotonic tensile results, the yield stress in the second stage tension is decreased by increasing the pre-strain and the intersection angle θ between two loading directions. Although the hardening rate is scarcely affected by θ, it can be decreased by increasing ε_{pre}. Influence of coarsening grain size is found to be weakening the effect induced by increasing ε_{pre} and θ, indicating that there are competitive processes between increasing the grain size d and changing the loading direction.

Table 4 Influences of the three parameters on the macro scale mechanical properties in the second stage tension.

Increasing the parameter	Influences on		
	Yield stress	Hardening rate	Elongation rate
θ	Decreasing	-	Decreasing
ε_{pre}	Decreasing	Decreasing	Decreasing
d	Weakening the effects above		Decreasing

3. Discussion

In order to shed light on the underlying mechanisms influenced by SPC and SE and provide basis for the physical-based constitutive modeling, electron backscattered diffraction (EBSD) was employed for microstructure characterization. Limited by the extremely thin thickness, specimen's tension-normal (RD-ND) section is polished and subjected to the characterization. A scanning electron microscope, NOVA NanoSEM 23, was used with the voltage of 20 kV and step size of 0.9 μm.

3.1 Effects of strain path change

Relative proportion of the main FCC crystal orientations, viz. (001), (101) and (111), are analyzed through the inverse pole figures (IPF) and distribution intensity. Stereographic projection on the upper hemisphere is adopted in analysis and the results are presented in Fig. 9. For the initial states of FG and CG specimens shown in Fig. 9 (a) and (e), the distribution gradients are similar with each other, though the (111) orientation is higher due to the recrystallization preference in annealing. After the first stage tension, both the orientation range and distribution are dramatically changed as shown in Fig. 9 (b) and (f). The intensity of (101) and its surrounding gradient are increased, revealing that the orientations tends to turn towards (101) when stretching along RD. Similar distribution is observed in CG specimens although the maximum intensity is located between (101) and (111).

Results measured after the second stage tension are plotted in Fig. 9 (c), (d), (g) and (h). In Fig. 9 (c), orientation with the maximum intensity gradually deviates from (101) to (001) after the second stage tension along DD. However, if the second stage loading is along TD, the maximum intensity tends to be located between (001) and (111). Comparing the results in Fig. 9 (b), (c) and (d), it can be concluded that the orientation preference introduced by first stage tension are reversed by the second stage tension along other directions and the deformation induced heterogeneity can be weakened by changing the subsequent strain path. Influences of SPC and SE on the

main slipping systems can be characterized by the Schmid factor evolution. For a certain deformation condition, each grain's Schmid factor was computed with regard to a given loading direction and the frequencies of the Schmid factor values could thus be calculated. After the normalization (based on the maximum frequency), the relative frequency of the Schmid factors are plotted in Fig. 10. according to the comparison between the black and blue curves (both referring to RD), the frequency of high Schmid factors (more than 0.4 shown as the shadow area) is decreased after the first stage tension. However, the results referring to other two directions (DD and TD) are increased according to the comparison between black and red lines or black and green lines.

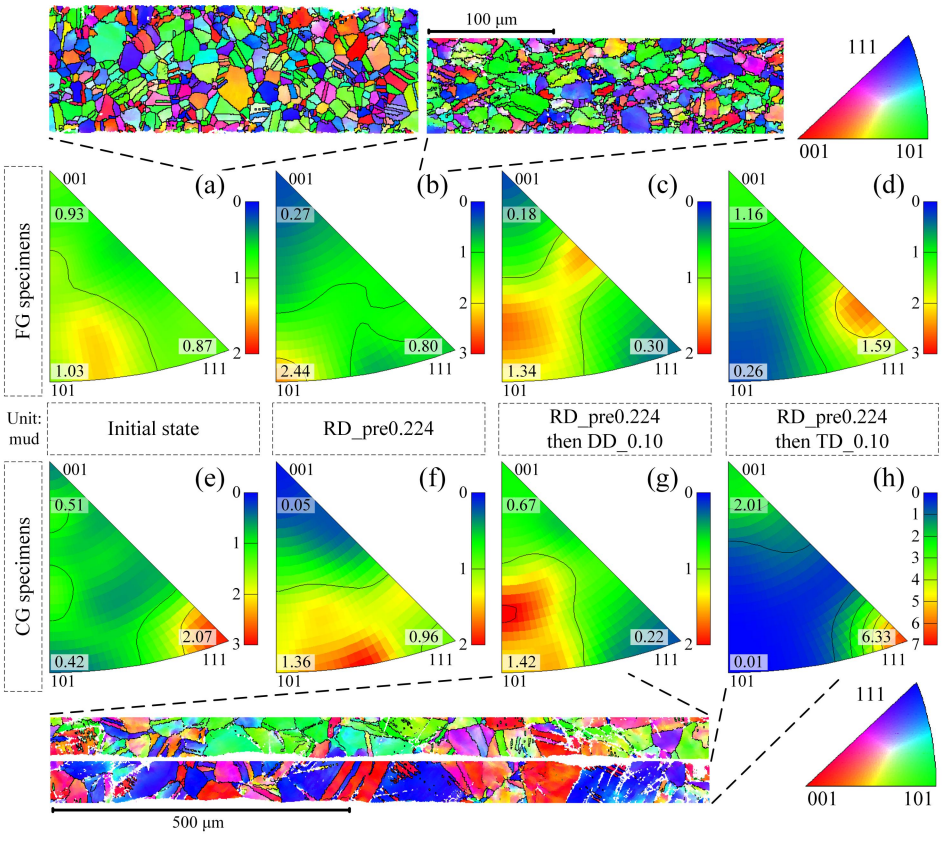

Fig. 9. Inverse pole figures and orientation intensity distribution of the initial and deformed specimens.

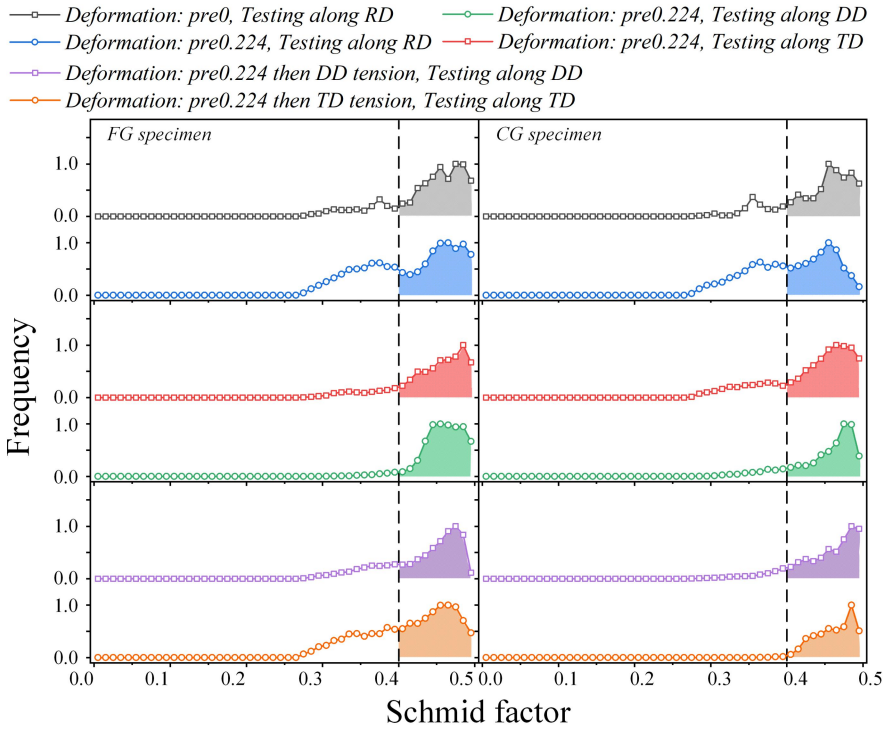

Fig. 10. The evolution of Schmid factor in FCC main slip system (111)[1$\bar{1}$0].

According to the experiment results listed in Table 4, enhancing the SPC loading e.g. increasing the ε_{pre} and θ lowers the yield stress and hardening rate, which can be attributed to the mechanism of the orientation distribution transformation and the Schmid factor evolution. As shown in Fig. 9, changing the loading direction in the second stage reverses the orientation intensity concentration. Besides, the evolution tendency in Fig. 10, indicates that the resistance of plastic deformation is continuously increased when stretching along the same direction but deformation along the other directions becomes easier to proceed. Owning to these micro scale mechanisms, both the yield stress and hardening rate are decreased in the second stage tension when the strain path is changed.

For CG specimens, similar orientation distribution patterns are observed in Fig. 9 (f), (g) and (h) but the intensity is much higher and concentrated, indicating that increasing the grain size contributes to the grains' orientation transformation. This is

attributed to the less restriction of the fewer grain boundaries when grains are coarsened. In that case, increasing the grain size is supposed to enhancing SPC's effects like lowering the yield stress and hardening rate. Nevertheless, the decreasing effect of SPC is weakened after the grain size is increased as summarized in Table 4, which implies that there is another confrontation effect of coarsening the grain size.

3.2 Influences of size effect

As shown in Fig. 3, more twinning strips are observed in TD-ND section and CG specimens attain higher twin density, which implies that the deformation along changed directions in the second stage tension bears different constraints due to the heterogeneous microstructure especially when the grain size is coarsened. Based on the EBSD characterization, the correlated misorientation angle distribution (MAD) is computed and relative frequencies of the angles are shown in Fig. 11. The curves are nearly identical in FG and CG specimens before deformation, indicating that their initial mismatching conditions are the same. However, the curves obviously diverge from each other and the frequency of low angle boundary (LAB) continuously increases with the strain [49]. LAB' frequency is obviously higher in CG specimens and so with the high angle boundary (HAB). After the first stage tension, the LAB frequency in CG specimen increases to 11.6% but the frequency in FG specimen is 7.8%. Although the difference in LAB frequency is reduced after the second stage tension, CG specimens still attain higher frequency of 5.5% than 4.3% for FG specimens. This indicates that the deformation heterogeneity inside the grains is enhanced with the grain coarsening, which correspondingly affects the macro and micro deformation behaviors in different grain size materials especially when SPC loading is performed.

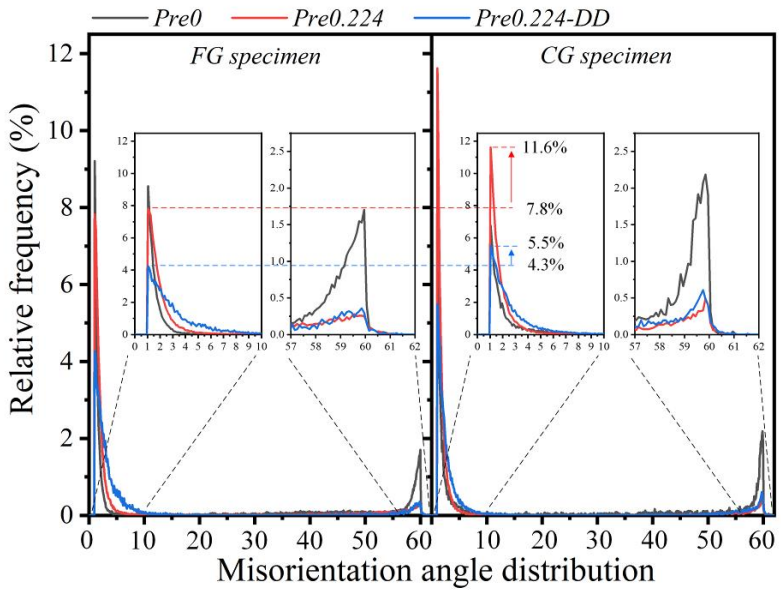

Fig. 11. Relative frequency of the correlated misorientation angle distribution.

As aforementioned, the drop of yield stress and hardening rate is supposed to be greater after coarsening. Nevertheless, the decrease turns out to be smaller, which owes to the deformation impediment induced by the mismatching boundaries inside grains. As shown in Fig. 11, coarse grains attain higher frequency of mismatching boundaries, so the impedance is correspondingly stronger in CG specimens. Areas with (101) orientation (preferred after the first stage tension) are extracted from the deformed specimens for detail comparison as shown in Fig. 12. Many mismatching boundaries spread inside the (101) oriented grains and coarse grains attains denser and higher angle distribution. The variation of mechanical properties such as the yield stress and hardening rate is dominated by the interactive influences of SPC and SE. Due to the increased Schmid factor, main slip systems are easier to be activated when the loading direction is changed in the second stage tension, so the flow stress and hardening rate are lowered consequently. On the other hand, deformation induced in-grain mismatching boundaries (more in coarse grains) impede the dislocation movement. So the force for activating the dislocation movement across these regions gets increased, which consequently minimizes the drop in yield stress and hardening

rate.

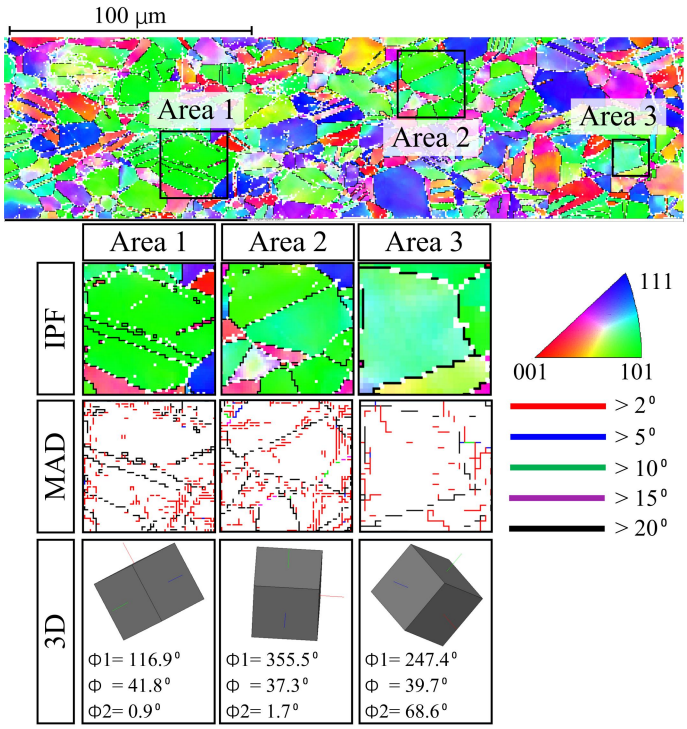
100 μm
Area 1
Area 2
Area 3
Area 1
Area 2
Area 3
IPF
MAD
3D
111
001
101
> 2°
> 5°
> 10°
> 15°
> 20°
Φ1= 116.9°
Φ = 41.8°
Φ2= 0.9°
Φ1= 355.5°
Φ = 37.3°
Φ2= 1.7°
Φ1= 247.4°
Φ = 39.7°
Φ2= 68.6°

(a)

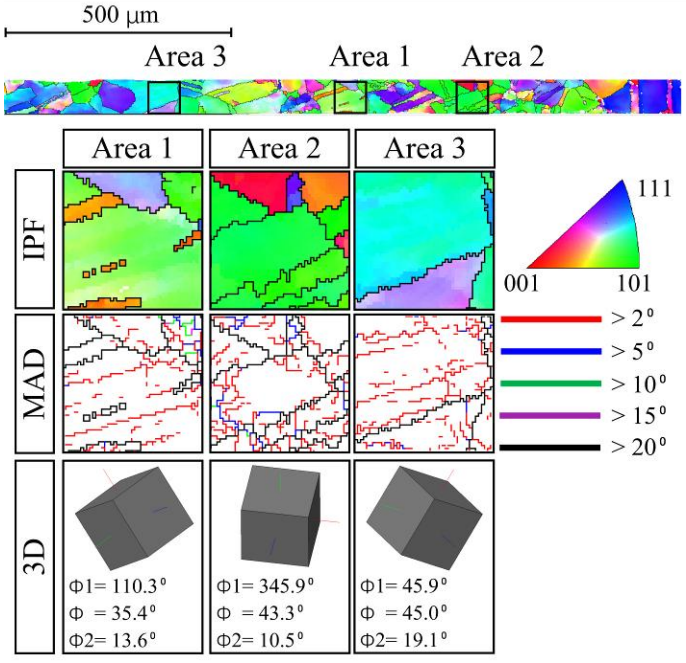
500 μm
Area 3
Area 1
Area 2
Area 1
Area 2
Area 3
IPF
MAD
3D
111
001
101
> 2°
> 5°
> 10°
> 15°
> 20°
Φ1= 110.3°
Φ = 35.4°
Φ2= 13.6°
Φ1= 345.9°
Φ = 43.3°
Φ2= 10.5°
Φ1= 45.9°
Φ = 45.0°
Φ2= 19.1°

(b)

Fig. 12. The comparison of MAD between areas with (101) orientation in specimens with 0.224 strain. a) results of FG specimens; b) results of CG specimens.

4. Constitutive models and validation

4.1 Constitutive modeling

Deformation of the ultra-thin metallic sheets is strongly affected by the size effect when the ratio of the grain size and specimen thickness is larger than the general threshold [1, 31]. In addition to that, abrupt strain path change is another indispensable factor influences the deformation behavior in the multi-stage forming [10, 44]. Based on the microstructure characterization results, a physical-based constitutive model considering both the SE and SPC is firstly established.

4.1.1 Modeling of size effect

Surface layer model assumes that the grains near the surface are less restricted so their properties can be approximately described by single crystal modeling. Correspondingly, the properties of the grains inside the material must be modeled following the polycrystalline governing. The material's flow stress can be expressed as:

$$H\left(\varepsilon_p\right)=\eta\sigma_{Sig}+\left(1-\eta\right)\sigma_{Pol} \tag{1}$$

where σ_{Sig} and σ_{Pol} are the flow stress for single crystal and polycrystalline [41]. η is the size effect factor evaluating the share of surface grains and it's calculated as the grains' average diameter d over the thickness t in sheet material [39]. According to the Hall-Petch relationship [50, 51], σ_{Sig} is related to the single crystal's critical resolved stress τ_R and σ_{Pol} is related to the interactions between grain boundaries and grain size:

$$\begin{cases}\sigma_{Sig} = m\tau_R \\ \sigma_{Pol} = M\tau_R + K_P/\sqrt{d}\end{cases} \tag{2}$$

where m is the reciprocal of the Schmid factor, M is an orientation related factor recommend to be 3.06 in polycrystalline material by Taylor [52] and K_P is the locally intensified stress required for propagating the yield across the polycrystalline grain boundaries. Substituting Eq. to , the material flow stress can be rewritten as:

$$H(\varepsilon_p) = (M - \eta M + \eta m)\tau_R + (1-\eta)K_P/\sqrt{d} \tag{3}$$

Both the critical resolved stress in single crystal and the flow stress in polycrystalline evolve with the increase of accumulated plastic strain. Under the influences of SE in micro forming, the composition of flow stress in sheet material can be expressed as [39]:

$$\begin{cases}\tau_R = \tau_0 + k_s \cdot \varepsilon_p^{n_s} \\ K_P = k_p \cdot \varepsilon_p^{n_p}\end{cases} \tag{4}$$

where τ_0 is the initial stress of very large grain, k_s and n_s are the strain hardening coefficient and exponent for single crystal, k_p and n_p are the analogical parameters for polycrystalline.

4.1.2 Modeling of strain path change

In addition to the size effect, the influences of pre-strain and loading direction must also be involved if the strain path is changed in complex micro forming. For polycrystalline materials, main slip systems with high Schmid factors mainly accommodate the plastic deformation. The percentage of the Schmid factor greater than 0.4 (as shown in Fig. 10) is defined as the high Schmid factor percentage (ψ) used to describe the high Schmid factor evolution. The Schmid factor is determined by the loading direction and the crystal orientation which are varying in SPC deformation: crystal orientations are correspondingly changed by the former stage deformation and the next stage loading direction also differs from the former one. To

address those issues, the evolution of Schmid factor must be described by parameters characterizing the deformation state of the former stage and the loading condition of the next stage. Influences of the SPC loading can be described in three manners: the plastic deformation amount of the former stage, the deformation induced anisotropy and the change of the loading direction in the next stage. Pre-strain (ε_{pre}) is used to quantifying the first manner, so the strain used for constitutive modeling is correspondingly rewritten as $\left(\varepsilon_p + \varepsilon_{pre}\right)$. For the other two manners, the SPC parameter δ [53] is employed for describing the coupled effect. A model capturing the high Schmid factor percentage ψ can thus be expressed as a state variable function $\psi\left(\varepsilon_{pre}, \delta\right)$.

The deformation induced anisotropy is represented by the r_θ defined as:

$$r_\theta = -\left(\varepsilon_b / \varepsilon_l\right) / \left(1 + \varepsilon_b / \varepsilon_l\right) \tag{5}$$

where ε_b and ε_l are the true strain along the transverse and longitude direction in actual loading. The change of loading direction is described by θ which attains values of $0°$, $45°$ and $90°$ in this study. The coupled effect of r_θ and θ can be represented by the SPC parameter calculated as:

$$\delta = \left(\dot{\mathbf{E}}_{\mathbf{pre}} : \dot{\mathbf{E}}_{\mathbf{sub}}\right) / \left(\left\|\dot{\mathbf{E}}_{\mathbf{pre}}\right\| \left\|\dot{\mathbf{E}}_{\mathbf{sub}}\right\|\right) \tag{6}$$

where $\dot{\mathbf{E}}_{\mathbf{pre}}$ is the rate of plastic deformation tensor of the first stage tension and $\dot{\mathbf{E}}_{\mathbf{sub}}$ is that of the subsequent stage tension. Taking the anisotropy into account [10], the rate of plastic deformation tensor can be expressed as a function of θ:

$$\dot{\mathbf{E}}_{\boldsymbol{\theta}} = \dot{\varepsilon}_\theta \begin{bmatrix} \cos^2\theta - \sin^2\theta \cdot r_\theta / \left(1 + r_\theta\right) & \cos\theta \sin\theta \cdot \left(1 + 2r_\theta\right) / \left(1 + r_\theta\right) & 0 \\ \cos\theta \sin\theta \cdot \left(1 + 2r_\theta\right) / \left(1 + r_\theta\right) & \sin^2\theta - \cos^2\theta \cdot r_\theta / \left(1 + r_\theta\right) & 0 \\ 0 & 0 & -1 / \left(1 + r_\theta\right) \end{bmatrix} \tag{7}$$

4.1.3 Hybrid constitutive model of SE and SPC

Deformation of the former stage changes gradually rotates the crystallographic plane's normal direction to the loading direction, so the Schmid factor is decreased and the yielding becomes harder to process. However, the loading direction is changed in the next stage deformation, so Schmid factor is correspondingly increased and the yielding across the grain boundaries can be enhanced. The overall average Schmid factor is increased when the percentage of high Schmid factors is raised, so the reciprocal of Schmid factor is negatively correlated to $\psi\left(\varepsilon_{pre},\delta\right)$ and m is modified as:

$$m = \omega_{Sig} - \zeta_{Sig} \cdot \psi\left(\varepsilon_{pre},\delta\right) \tag{8}$$

where ω_{Sig} and ζ_{Sig} are material parameters determining the initial and evolving coefficients in strain path change loading. For the polycrystalline stress, the yielding across the grain boundaries is also lowered and expressed as:

$$k_p = \omega_{Pol} - \zeta_{Pol} \cdot \psi\left(\varepsilon_{pre},\delta\right) \tag{9}$$

where ω_{Pol} and ζ_{Pol} is the evolving coefficient influenced by the grain/subgrain boundaries in polycrystalline. The parameters of the hybrid constitutive model accounting for the SE and SPC can be identified following 4 steps:

(1) Calibrating the SE factor η based on the metallography or microstructure characterization.

(2) Computing the SPC parameter δ from the measured r and θ in the two-stage tensile tests.

(3) Determining the evolution function $\psi\left(\varepsilon_{pre},\delta\right)$ according to the Schmid factor statistic results obtained in the EBSD tests.

(4) Estimating the parameters τ_0, k_s, n_s, n_p, ω_{Sig}, ζ_{Sig}, ω_{Pol} and ζ_{Pol} from the stress-strain curves of two-stage tensile tests with different grain size specimens by using the least square method (LSM).

4.2 Parameter identification

4.2.1 Evolution of the SPC parameter

By using the DIC measurement, the transverse strain ε_b and longitude strain ε_l can be obtained simultaneously and the results are plotted in Fig. 13. The calculated r_θ and δ with regard to θ in the monotonic and two-stage tensile tests are listed in Table 5 and 6. Although the commercial SS 316L sheets are rolling produced, the anisotropy is almost eliminated by annealing as the initial r-values along three directions are similar. For FG specimens, the r-values in second stage tension are increased with pre-strain and reach the peaks at around $\theta = 45^o$ [10]. However, the tendencies in CG specimens are weakened and the r-values along DD and TD are even quite similar with each other, which is in accordance with the results summarized in Table 4.

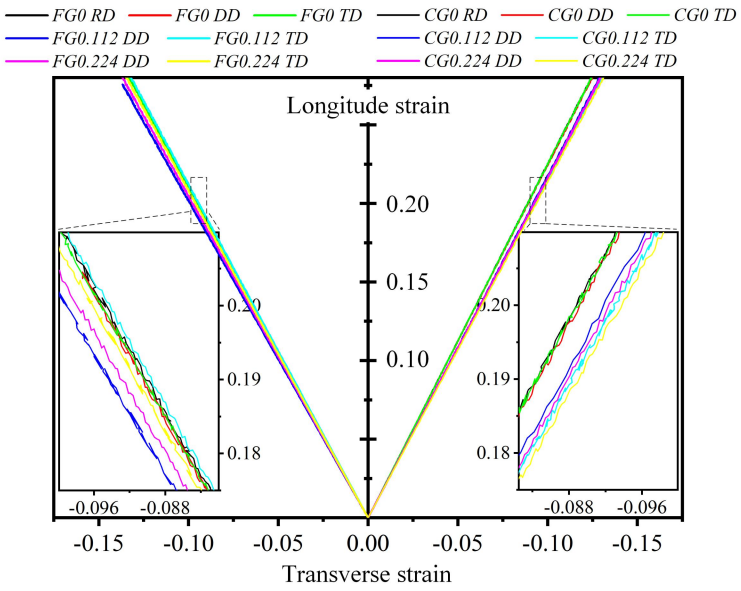

Fig. 13. The transverse and longitude strain curves measured by DIC.

For FG specimens loaded along DD, δ is only slightly changed from 0.2650 to 0.2635, despite of the fact that the pre-strain is doubled. Similar results can be found

in other conditions, so the pre-strain rarely influences δ. According to the definition of δ, the monotonic, cross and reverse loadings correspond to δ=1,0,-1, respectively [10]. In this study, δ is changed from about 0.26 to -0.45, indicating that these two-stage tensile experiments cover a sufficient range of SPC loading conditions with a good representativeness.

Table 5 r-value and δ in the experiments of fine grain specimens

r-value			δ	
1st tension	2nd tension		Pre-strain 0.112	Pre-strain 0.224
	Pre-strain 0.112	Pre-strain 0.224		
r_{0^o} = 0.9009	-	-	δ_{0^o} = 1.0	δ_{0^o} = 1.0
r_{45^o} = 0.9356	r_{45^o} = 0.9845	r_{45^o} = 0.9956	δ_{45^o} = 0.2650	δ_{45^o} = 0.2635
r_{90^o} = 0.9164	r_{90^o} = 0.8925	r_{90^o} = 0.9247	δ_{90^o} = -0.4446	δ_{90^o} = -0.4537

Table 6 r-value and δ in the experiments of coarse grain specimens

r-value			δ	
1st tension	2nd tension		Pre-strain 0.112	Pre-strain 0.224
	Pre-strain 0.112	Pre-strain 0.224		
r_{0^o} = 0.7896	-	-	δ_{0^o} = 1.0	δ_{0^o} = 1.0
r_{45^o} = 0.8151	r_{45^o} = 0.8697	r_{45^o} = 0.8853	δ_{45^o} = 0.2979	δ_{45^o} = 0.2962
r_{90^o} = 0.8032	r_{90^o} = 0.8654	r_{90^o} = 0.8778	δ_{90^o} = -0.4024	δ_{90^o} = -0.4047

4.2.2 Evolution of the Schmid factor

The high Schmid factor percentage ψ of the main slipping systems viz. (111)[$1\bar{1}0$], is presented in Fig. 14. After the first stage deformation, the ψ referring to RD is decreased but the percentages with regard to DD and TD are increased.

Similar dropping is observed along DD and TD when the second stage tension is conducted. The correlation between ψ and the SPC parameter δ is well represented by a parabola function as shown in Fig. 15. Since the pre-strain remained after the first stage loading is the prerequisite to the SPC loading, the evolution of ψ is proposed to be:

$$\psi\left(\varepsilon_{pre},\delta\right)=\varepsilon_{pre}\left(1-\delta\right)^{2} \tag{10}$$

Along with the parameters ω_{Sig} and ζ_{Sig} (ω_{Pol} and ζ_{Pol} for polycrystalline) which describes the initial and evolving coefficients, the hybrid constitutive model can be obtained by substituting into Eq.s and .

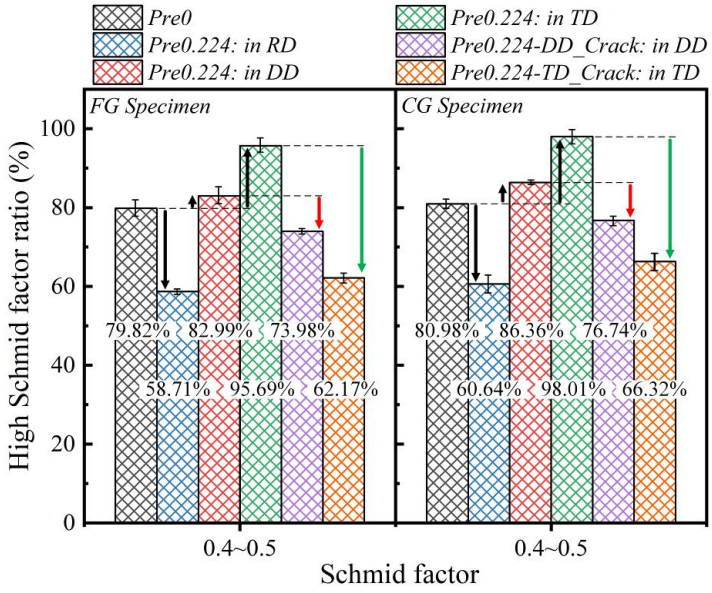

Fig. 14. The high Schmid factor percentage in (111)[1$\bar{1}$0] slipping systems under different loading conditions.

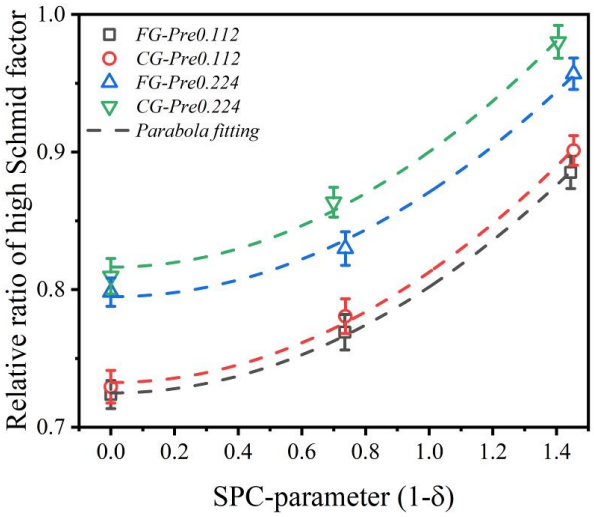

Fig. 15. Evolution of the high Schmid factor percentage in two-stage tension. The SPC parameter is designated as the function (1-δ).

4.3 Validation of the hybrid constitutive model

The flow stress of specimens influenced by SE and SPC can be computed based on the hybrid constitutive model. Performances of the conventional Swift hardening model (as designated in Table 2) and the model proposed by Lai et. al [39] (as designated in Table 7) are used for comparison. The models' parameters identified based on the monotonic and two-stage tensile tests (ε_{pre} 0.112-DD & ε_{pre} 0.224-TD) are listed in Table 7 and the predicted flow stress of the two-stage tensile tests is shown in Fig. 16.

Table 7 The identified parameters of the constitutive models.

Lai et. al $\sigma=(\eta m-\eta M+M)\left(k_1+k_2\varepsilon_p^{\ k_3}\right)+(1-\eta)k_4\varepsilon_p^{\ k_5}$								
k_1	k_2		k_3		k_4		k_5	
76.88	677.95		1.01		21.25		0.23	
Proposed model	τ_0	k_s	n_s	n_p	ω_{Sig}	ζ_{Sig}	ω_{Pol}	ζ_{Pol}
	71.30	346.07	0.66	0.19	2.50	0.50	13.81	31.44

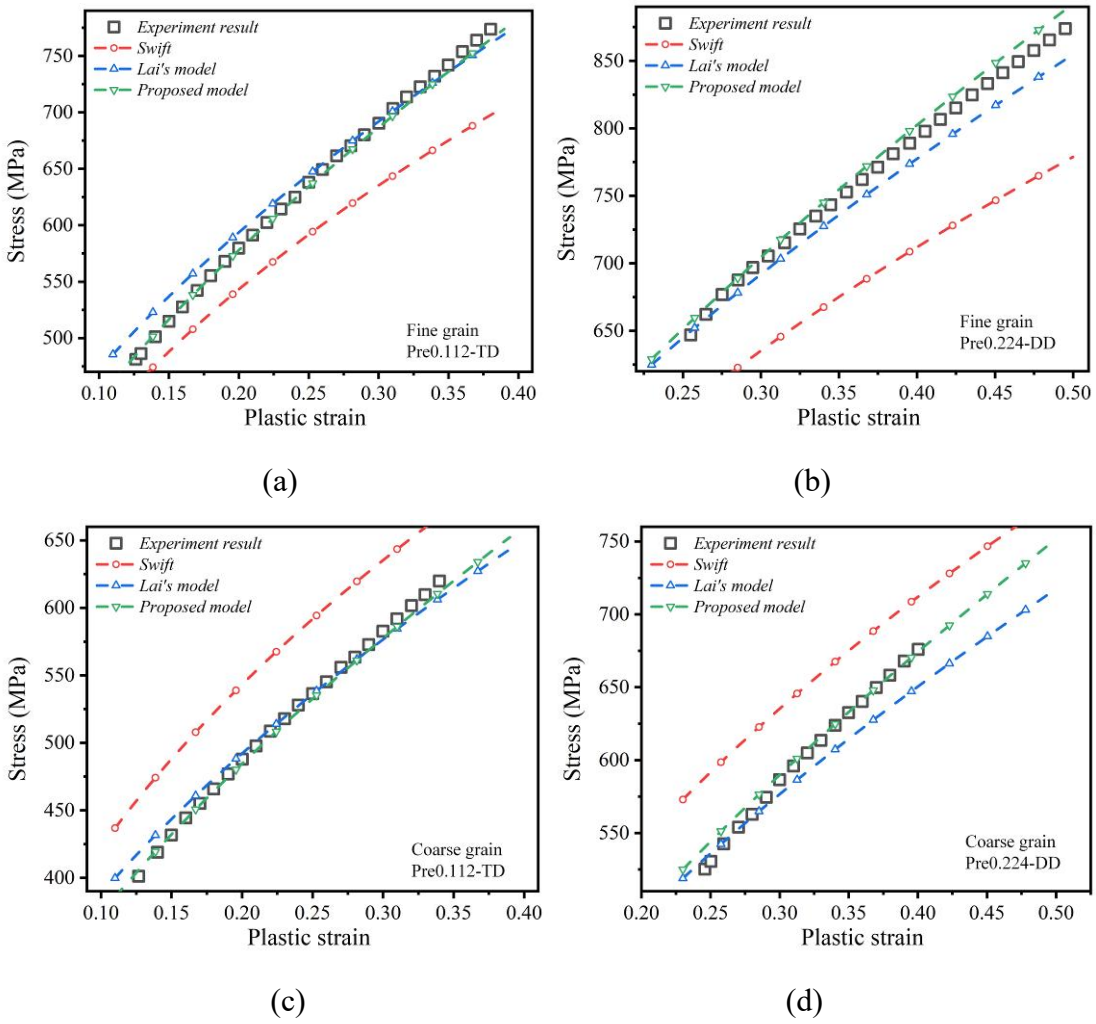

Fig. 16. Performance in predicting the flow stress of the two-stage tensile tests. (a) and (b) are results of FG specimens; (c) and (d) are the results of CG specimens.

Swift hardening fails in predicting the flow stress of the second stage tension. Lai's model which involves the surface layer theory, predicts the flow stress of the specimens with different grain sizes well, but it is only effective in monotonic tension. The proposed hybrid model in this research, however, shows a good agreement with the experiment results, because the SPC parameter and pre-strain are both employed for describing the effects of strain path change. This model is adequate to characterize the flow stress of the ultra-thin metallic sheets with different grain sizes in two-stage tension.

The hybrid model's performance in describing the influences of pre-strain, SPC

parameter and size factor are analyzed. Three levels of pre-strain (along RD) and size factor are used and the evolution of yield stress are presented with SPC parameter decreasing from 1 (standing for pure monotonic tension) to -1 (standing for complete tension-compression loading). Fixing the additional strain in the second stage as 0.1, the computed results are plotted in Fig. 17 where the radial direction measures the yield stress and the angular direction measures the SPC parameter linearly. As the pre-strain increases, the yield stress in the second stage is overall increased but the increment is decreased with the increasing of size factor, viz. coarsening the grains. With the decreasing of SPC parameter, the decrease of the yield stress is prompted. On the other hand, the drop of yield stress induced by minimizing the SPC parameter is slowed down by increasing the size factor. The performance of the yield stress evolution coincides with the experiment results well, which validates that the proposed hybrid model is capable to capture the features of stress-strain relationship in two-stage tensile tests.

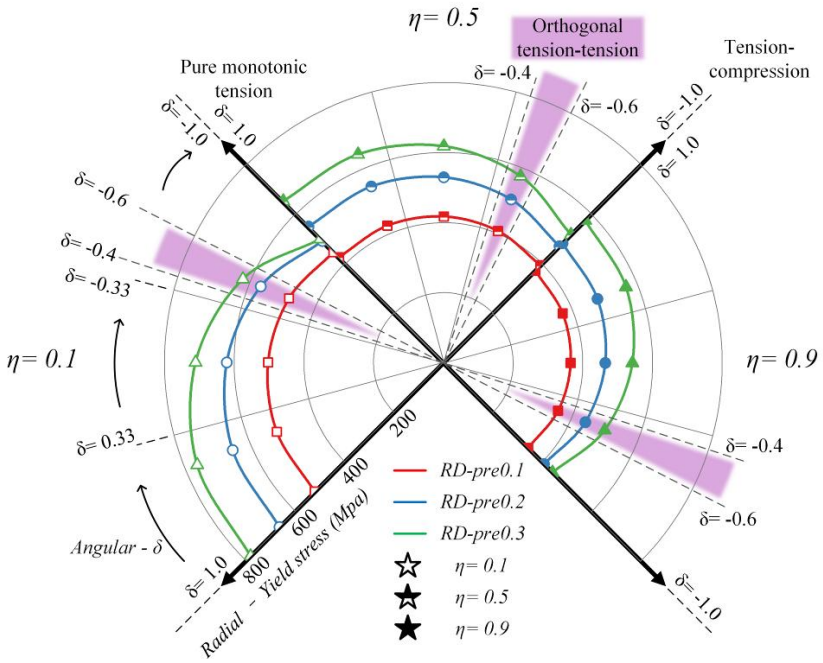

Fig. 17. Evolution of the hybrid model with varied pre-strain, SPC parameter and size factor.

4.4 Implementation in micro channel forming

The manufacturing of micro channels with the width of 1.0 mm was done for validating the application of the hybrid model. For comparison, Swift hardening model (as designated in Table 2), Lai's model (as designated in Table 7) and the proposed hybrid model in this research were used for the prediction of the deformation force in two-stage forming of micro channels with ultra-thin sheets. The commercial FEA software Abaqus and its UMAT subroutine were used for simulation. Voronoi Tessellation Method was used to randomly divide the sheet into aggregated individual cells and each cell represents a single grain. By controlling the cells' average size, two types of ultra-thin sheets with the grain sizes of 21.5 (as FG specimen) and 74.6 μm (as CG specimen) were established. The grains were also randomly assigned with three typical orientations viz. 0°, 45°, 90° (referred to the sheets rolling direction) in the user defined material constant. Based on the corresponding grain size and the orientation, each grain's stress-strain response can thus be determined following the proposed hybrid model in the UMAT coding. Limited by the Voronoi tessellation efficiency, 3D deformable part with the dimensions of 7.0 (length-X) × 0.1 (thickness-Y) × 1.0 mm (width-Z) was built for representing the ultra-thin sheet as shown in Fig. 18. Although only three grooves are formed in the simulation, it is sufficient to validate the models' performance with the symmetrical boundary conditions. As illustrated in Fig. 18, the tool's ridge widths and clearances are set as 0.85 mm and 0.15 mm respectively and the fillet radius is set as 0.42 and 0.15 mm for the first and second stage. All the faces of the specimen are symmetrically constrained except the upper and lower faces which contact with the tool surface. The friction coefficient between the sheet and the tools was set as 0.1. C3D8 element was used and at least five elements along thickness direction were ensured. Four virtual blocks were used for preventing specimen's unexpected motion during tool alternation and a tiny spacing between the specimen and blocks was released to avoid redundant force. Via controlling the punch displacement as 0.7 and

0.6 mm in each stage, the two-stage forming was performed by deforming the ultra-thin sheet with the two tool sets consecutively.

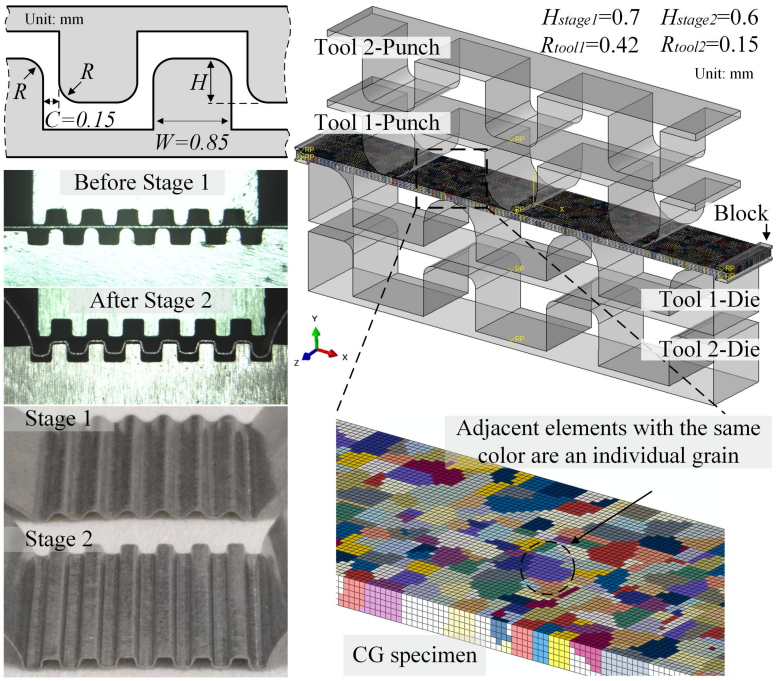

Fig. 18. Schematic of the experiment and simulation setup.

A UMAT subroutine was developed based on the proposed constitutive model. The implicit/standard solver of commercial FEA software Abaqus was used and the flow chart of the stress updating algorithm is presented in Fig. 19. The standard radial-return mapping algorithm was adopted in the calculation. In each calculation time increment, the strain increment tensor $\mathbf{\Delta\varepsilon}_{n+1}$ can be decomposed as:

$$\mathbf{\Delta\varepsilon}_{n+1} = \mathbf{\Delta\varepsilon}^{el}_{n+1} + \mathbf{\Delta\varepsilon}^{pl}_{n+1} \tag{17}$$

where the subscript $(n+1)$ denotes the increment sequence, the superscript el and pl represent the elastic part and plastic part. $\mathbf{\Delta\varepsilon}_{n+1}$ is initially assumed to be totally elastic, so the trial stress $\mathbf{\sigma}^{T}_{n+1}$ in current increment can be calculated as:

$$\mathbf{\sigma}^{T}_{n+1} = \mathbf{D}^{el} : \left(\mathbf{\varepsilon}_{n} + \mathbf{\Delta\varepsilon}_{n+1}\right) \tag{18}$$

where $\mathbf{D}^{el}$ is the elastic modulus tensor formed based on the elastic modulus E and

Poission ratio ν. The trial stress was then used to determine whether the material yields. If so, the intersection angle θ will be calculated based on the previous loading direction (RD in this simulation) and the grain orientation:

1) If $\theta = 0$, no strain path change is imposed and the hybrid model regresses to the surface layer model. The material constants $\tau_0, k_s, n_s, n_p, \omega_{pol}$, grain size d and grain size factor η govern the hardening function $H\left(\varepsilon_p\right)$ for computing the actual stress σ_{n+1} in the current time increment.
2) If $\theta \neq 0$, strain path change is imposed in the deformation and the plastic strain remained after the first stage loading is taken as the pre-strain. Both θ and η are used to calculate the SPC parameter δ for building $\psi\left(\varepsilon_{pre}, \delta\right)$. The material constants $\tau_0, k_s, n_s, n_p, \omega_{sig}, \zeta_{sig}, \omega_{pol}, \zeta_{pol}, d, \eta$ and $\psi\left(\varepsilon_{pre}, \delta\right)$ govern the hardening function $H\left(\varepsilon_p\right)$ for computing σ_{n+1}.

Based on the associated flow rule, the plastic flow multiplier $d\lambda$ can obtained via Newton-Raphson iteration. The actual plastic strain increment can be determined by using $d\lambda$ and thus σ_{n+1} can be calculated and used to be compared with the flow stress σ_{new}^{0} under current plastic strain. Once the consistency condition is satisfied, the variables calculated based on the current $d\lambda$ will be used to compute the consistent tangent modulus and Jacobian matrix. After transforming these variable results to the main program, the current time increment calculation is finished.

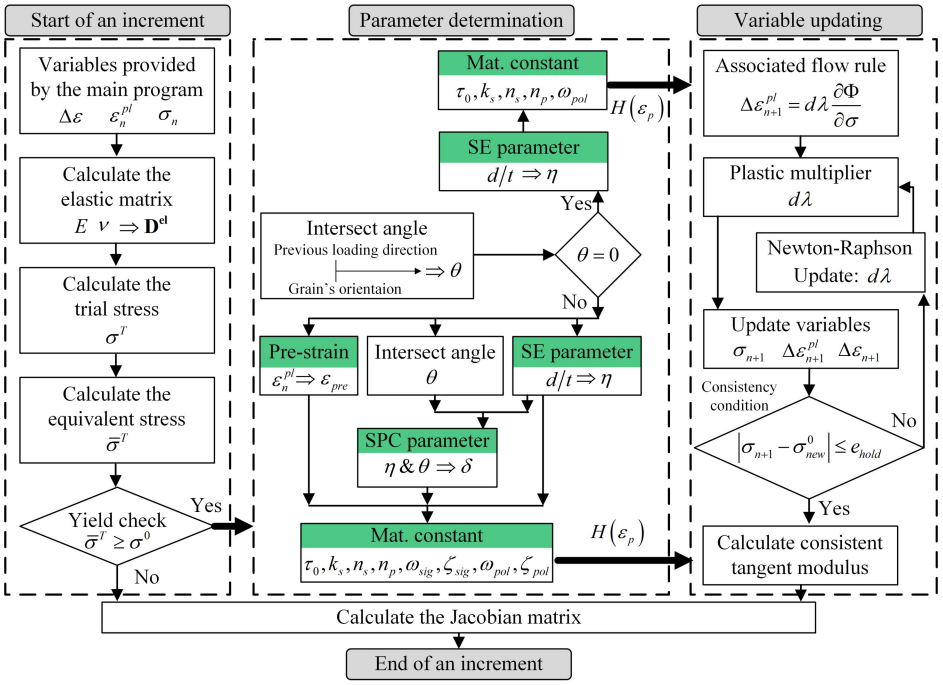

Fig. 19. The flow chart of stress updating algorithm.

As plotted in Fig. 20, the predicted forming force in two stages is compared with the experiment results. Since the real specimen's width (10.0 mm) was ten times of the simulation specimen's width and seven channels were formed in experiments, the simulation results were magnified ten times and experiment forming force were also linearly reduced from seven to three channels before comparison. For the first stage, the simulations results show a good agreement with the experimental results. The strain path is not changed owning to the fully rounded forming tools, so the proposed model regresses to only considering the grain size effect and thus presents almost the same results with Lai's model. Tools with a smaller radius were employed in the second stage, so the strains in the regions which sequentially contact with the tool fillet corners is correspondingly changed. The Swift hardening model overestimates the forming forcing which increases dramatically with the punch stroke. Although the results of Lai's model are closer to the experimental results than Swift hardening model's prediction, it gradually deviates from the real forming force as the deformation proceeds. Compared to the former two models, the proposed hybrid

model presents a sufficient accuracy and the variation trend of the deformation force predicted by the proposed model is also quite close to the experimental results, revealing that the consideration of strain path change in multi-stage micro forming is essential and the efficiency of proposed model is validated.

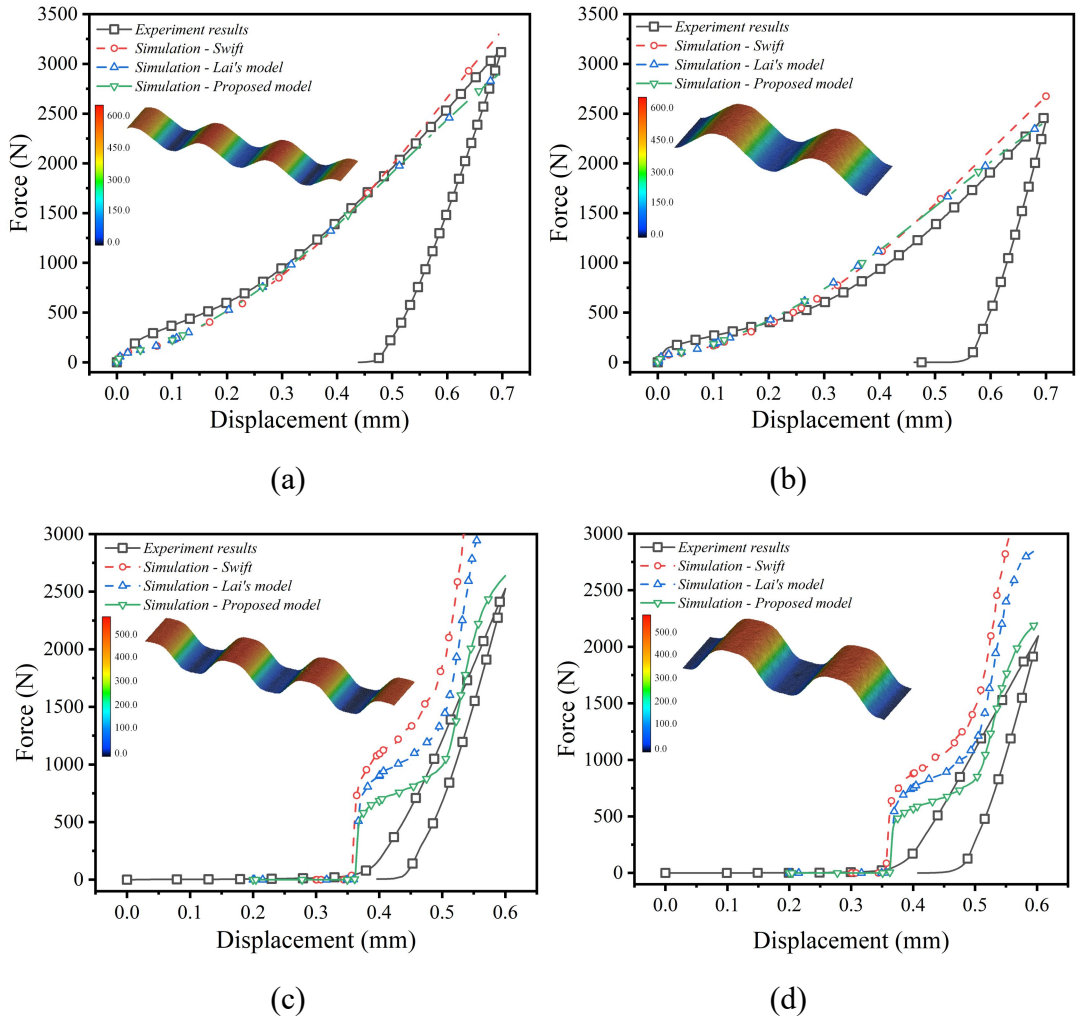

Fig. 20. Comparison of the simulation predicted and the experimental forming force of the two-stage micro channel forming. (a) FG specimen in stage one; (b) CG specimen in stage one; (c) FG specimen in stage two; (d) CG specimen in stage two. The 3D pictures are the corresponding channel profile scanned by Keyence VK-X250.

5. Conclusion

The deformation behaviors of the ultra-thin metallic sheets under strain path

change (SPC) loading with the grain size effect (SE) were systematically studied through the two-stage tensile deformation. The influences of SPC and SE on microstructure evolution were thoroughly analyzed at grain level, which provided an in-depth understanding of the underlying mechanisms affected by SPC and SE. A constitutive model considering the influences of SPC and SE was established based on the SPC parameter and grain size factor. The prediction of the stress-strain relationship showed a good agreement with the results of the two-stage tension and two-stage micro channel forming with ultra-thin metallic sheets. The following concluding remarks are thus obtained:

1) Reloading yield stress and elongation rate in the second stage is decreased when ε_{pre} (pre-strain) and θ (the interaction angle between two loading directions) is increased. The r-value is also decreased with the increasing θ, but increased with ε_{pre}. θ is found to be scarcely influencing the hardening rate which is decreased by increasing ε_{pre} solely.

2) Orientation preference after the first stage tension is gradually reversed with the increase of θ and coarsening grains enhances this reverse effect. Mismatching boundaries are increased with the deformation and they attain higher densities in coarse grain specimens.

3) The high Schmid factor percentage is increased by changing strain path, so the yield stress and hardening rate are thus decreased in SPC loading. On the other hand, more mismatching boundaries accumulated in the coarsened grains, which impedes the dislocation motion and raises the flow stress. The confrontation effects of SPC and SE interactively influence the stress-strain relationship in multi-stage deformation.

4) Although the SPC parameter is rarely influenced by the pre-strain, it increases with minimizing θ or coarsening the grains. The percentage of high Schmid factor in 316L ultra-thin sheets with FCC matrix is found to be evolving with the pre-strain

and the SPC parameter in a quadratic manner. These relationships are correspondingly employed in the physical-based constitutive modeling.

5) Constitutive modeling of both the SPC and SE was conducted based on the micro-scaled mechanisms for the first time. The hybrid model is capable to predict the flow stress of ultra-thin sheets with different grain sizes and the deformation force of the micro channel multi-stage forming with a satisfactory accuracy and efficiency.

References

[1] M.W. Fu, W.L. Chan, A review on the state-of-the-art microforming technologies, The International Journal of Advanced Manufacturing Technology, 67 (2013) 2411-2437. https://doi.org/10.1007/s00170-012-4661-7.

[2] X.M. Lai, M.W. Fu, L.F. Peng, Sheet Metal Meso-and Microforming and Their Industrial Applications, CRC Press, 2018.

[3] L. Peng, P. Yi, X. Lai, Design and manufacturing of stainless steel bipolar plates for proton exchange membrane fuel cells, International Journal of Hydrogen Energy, 39 (2014) 21127-21153. https://doi.org/10.1016/j.ijhydene.2014.08.113.

[4] M.M. Barzegari, F.A. Khatir, Study of thickness distribution and dimensional accuracy of stamped metallic bipolar plates, International Journal of Hydrogen Energy, 44 (2019) 31360-31371. https://doi.org/10.1016/j.ijhydene.2019.09.225.

[5] Z. Wu, Q. Cao, J. Fu, Z. Li, Y. Wan, Q. Chen, L. Li, X. Han, An inner-field uniform pressure actuator with high performance and its application to titanium bipolar plate forming, International Journal of Machine Tools and Manufacture, 155 (2020) 103570. https://doi.org/10.1016/j.ijmachtools.2020.103570.

[6] H.J. Bong, J.W. Lee, J.H. Kim, F. Barlat, M.G. Lee, Two-stage forming approach for manufacturing ferritic stainless steel bipolar plates in PEM fuel cell: Experiments and numerical simulations, International Journal of Hydrogen Energy, 42 (2017) 6965-6977. https://doi.org/10.1016/j.ijhydene.2016.12.094.

[7] Z. Xu, Z. Li, R. Zhang, T. Jiang, L. Peng, Fabrication of micro channels for titanium PEMFC bipolar plates by multistage forming process, International Journal of Hydrogen Energy, (2020). https://doi.org/10.1016/j.ijhydene.2020.07.230.

[8] H.J. Bong, F. Barlat, J.W. Lee, M.G. Lee, J.H. Kim, Application of central composite design for optimization of two-stage forming process using ultra-thin ferritic stainless steel, Metals and Materials International, 22 (2016) 276-287. https://doi.org/10.1007/s12540-015-4325-x.

[9] R. Zhang, S.H. Lan, Z.T. Xu, D.K. Qiu, L.F. Peng, Investigation and optimization of the ultra-thin metallic bipolar plate multi-stage forming for proton exchange membrane fuel cell, Journal of Power Sources, 484 (2021) 229298. https://doi.org/10.1016/j.jpowsour.2020.229298.

[10] J.J. Ha, M.G. Lee, F. Barlat, Strain hardening response and modeling of EDDQ and DP780 steel sheet under non-linear strain path, Mechanics of Materials, 64 (2013) 11-26. https://doi.org/10.1016/j.mechmat.2013.04.004.
[11] M.W. Fu, J.L. Wang, A.M. Korsunsky, A review of geometrical and microstructural size effects in micro-scale deformation processing of metallic alloy components, International Journal of Machine Tools and Manufacture, 109 (2016) 94-125. https://doi.org/10.1016/j.ijmachtools.2016.07.006.
[12] Z. Chang, M. Li, J. Chen, Analytical modeling and experimental validation of the forming force in several typical incremental sheet forming processes, International Journal of Machine Tools and Manufacture, 140 (2019) 62-76. https://doi.org/10.1016/j.ijmachtools.2019.03.003.
[13] Z. Yang, W. Xu, H. Wu, X. Wan, Y. Chen, D. Shan, B. Guo, Enhancing hoop strength of titanium alloy tube by cross spinning, International Journal of Machine Tools and Manufacture, 152 (2020) 103530. https://doi.org/10.1016/j.ijmachtools.2020.103530.
[14] H. Su, L. Huang, J. Li, F. Ma, P. Huang, F. Feng, Two-step electromagnetic forming: A new forming approach to local features of large-size sheet metal parts, International Journal of Machine Tools and Manufacture, 124 (2018) 99-116. https://doi.org/10.1016/j.ijmachtools.2017.10.005.
[15] H. Kim, F. Barlat, Y. Lee, S.B. Zaman, C.S. Lee, Y. Jeong, A crystal plasticity model for describing the anisotropic hardening behavior of steel sheets during strain-path changes, International Journal of Plasticity, 111 (2018) 85-106. https://doi.org/10.1016/j.ijplas.2018.07.010.
[16] F. Yoshida, T. Uemori, K. Fujiwara, Elastic–plastic behavior of steel sheets under in-plane cyclic tension–compression at large strain, International Journal of Plasticity, 18 (2002) 633-659. http://doi.org/10.1016/S0749-6419(01)00049-3.
[17] E. Silvestre, J. Mendiguren, L. Galdos, E. Sáenz de Argandoña, Comparison of the hardening behaviour of different steel families: From mild and stainless steel to advanced high strength steels, International Journal of Mechanical Sciences, 101–102 (2015) 10-20. http://dx.doi.org/10.1016/j.ijmecsci.2015.07.013.
[18] R. Zhang, Z. Xu, Y. Deng, L. Peng, Characterizing the back stress of ultra-thin metallic sheet via pre-strain tension/bending process, Journal of Materials Processing Technology, 279 (2020) 116560. https://doi.org/10.1016/j.jmatprotec.2019.116560.
[19] J. Bauschinger, Ueber die Veranderung der Elasticitatagrenze und dea Elasticitatamoduls verschiadener Metalle, Zivilingenieur, (1881) 289-348.
[20] K. Yoshida, T. Tsuchimoto, Plastic flow of thin-walled tubes under nonlinear tension-torsion loading paths and an improved pseudo-corner model, International Journal of Plasticity, 104 (2018) 214-229. https://doi.org/10.1016/j.ijplas.2018.02.013.
[21] K.H. Kim, J.J. Yin, Evolution of anisotropy under plane stress, Journal of the Mechanics and Physics of Solids, 45 (1997) 841-851. https://doi.org/10.1016/S0022-5096(96)00085-3.
[22] Z.Y. Cai, B. Meng, M. Wan, X.D. Wu, M.W. Fu, A modified yield function for

modeling of the evolving yielding behavior and micro-mechanism in biaxial deformation of sheet metals, International Journal of Plasticity, 129 (2020) 102707. https://doi.org/10.1016/j.ijplas.2020.102707.
[23] T.S. Yang, The strain path and forming limit analysis of the lubricated sheet metal forming process, International Journal of Machine Tools and Manufacture, 47 (2007) 1311-1321. https://doi.org/10.1016/j.ijmachtools.2006.08.019.
[24] T.B. Stoughton, J.W. Yoon, Path independent forming limits in strain and stress spaces, International Journal of Solids and Structures, 49 (2012) 3616-3625. https://doi.org/10.1016/j.ijsolstr.2012.08.004.
[25] K. Sofinowski, T. Panzner, M. Kubenova, J. Čapek, S. Van Petegem, H. Van Swygenhoven, In situ tension-tension strain path changes of cold-rolled Mg AZ31B, Acta Materialia, 164 (2019) 135-152. https://doi.org/10.1016/j.actamat.2018.10.033.
[26] X.F. Xie, W.C. Jiang, J.K. Chen, X.C. Zhang, S.T. Tu, Cyclic hardening/softening behavior of 316L stainless steel at elevated temperature including strain-rate and strain-range dependence: Experimental and damage-coupled constitutive modeling, International Journal of Plasticity, 114 (2019) 196-214. https://doi.org/10.1016/j.ijplas.2018.11.001.
[27] J.S. Qin, B. Holmedal, K. Zhang, O.S. Hopperstad, Modeling strain-path changes in aluminum and steel, International Journal of Solids and Structures, 117 (2017) 123-136. https://doi.org/10.1016/j.ijsolstr.2017.03.032.
[28] W. Wen, M. Borodachenkova, C.N. Tomé, G. Vincze, E.F. Rauch, F. Barlat, J.J. Grácio, Mechanical behavior of Mg subjected to strain path changes: Experiments and modeling, International Journal of Plasticity, 73 (2015) 171-183. https://doi.org/10.1016/j.ijplas.2014.10.009.
[29] W. He, T. Lin, Q. Liu, Experiments and constitutive modeling of deformation behavior of a magnesium sheet during two-step loading, International Journal of Solids and Structures, 147 (2018) 52-60. https://doi.org/10.1016/j.ijsolstr.2018.04.009.
[30] S.B. Zaman, F. Barlat, J.-H. Kim, Deformation-induced anisotropy of uniaxially prestrained steel sheets, International Journal of Solids and Structures, 134 (2018) 20-29. https://doi.org/10.1016/j.ijsolstr.2017.10.029.
[31] M. Geiger, M. Kleiner, R. Eckstein, N. Tiesler, U. Engel, Microforming, CIRP Annals, 50 (2001) 445-462. https://doi.org/10.1016/S0007-8506(07)62991-6.
[32] X. Lai, H. Li, C. Li, Z. Lin, J. Ni, Modelling and analysis of micro scale milling considering size effect, micro cutter edge radius and minimum chip thickness, International Journal of Machine Tools and Manufacture, 48 (2008) 1-14. https://doi.org/10.1016/j.ijmachtools.2007.08.011.
[33] S. Mahabunphachai, M. Koç, Investigation of size effects on material behavior of thin sheet metals using hydraulic bulge testing at micro/meso-scales, International Journal of Machine Tools and Manufacture, 48 (2008) 1014-1029. https://doi.org/10.1016/j.ijmachtools.2008.01.006.
[34] M.W. Fu, W.L. Chan, Geometry and grain size effects on the fracture behavior of sheet metal in micro-scale plastic deformation, Materials & Design, 32 (2011)

4738-4746. https://doi.org/10.1016/j.matdes.2011.06.039.
[35] Z. Xu, L. Peng, E. Bao, Size effect affected springback in micro/meso scale bending process: Experiments and numerical modeling, Journal of Materials Processing Technology, 252 (2018) 407-420. https://doi.org/10.1016/j.jmatprotec.2017.08.040.
[36] M.A. Meyersm, E. Ashworth, A model for the effect of grain size on the yield stress of metals, Philosophical Magazine A, 46 (1982) 737-759. https://doi.org/10.1080/01418618208236928.
[37] X.F. Tang, S.Q. Shi, M.W. Fu, Interactive effect of grain size and crystal structure on deformation behavior in progressive micro-scaled deformation of metallic materials, International Journal of Machine Tools and Manufacture, 148 (2020) 103473. https://doi.org/10.1016/j.ijmachtools.2019.103473.
[38] X.X. Chen, A.H.W. Ngan, Specimen size and grain size effects on tensile strength of Ag microwires, Scripta Materialia, 64 (2011) 717-720. https://doi.org/10.1016/j.scriptamat.2010.12.031.
[39] X.M. Lai, L.F. Peng, P. Hu, S.H. Lan, J. Ni, Material behavior modelling in micro/meso-scale forming process with considering size/scale effects, Computational Materials Science, 43 (2008) 1003-1009. https://doi.org/10.1016/j.commatsci.2008.02.017.
[40] U. Engel, R. Eckstein, Microforming—from basic research to its realization, Journal of Materials Processing Technology, 125-126 (2002) 35-44. https://doi.org/10.1016/S0924-0136(02)00415-6.
[41] L.F. Peng, X.M. Lai, H.J. Lee, J.H. Song, J. Ni, Analysis of micro/mesoscale sheet forming process with uniform size dependent material constitutive model, Materials Science and Engineering: A, 526 (2009) 93-99. https://doi.org/10.1016/j.msea.2009.06.061.
[42] Z.T. Xu, L.F. Peng, M.W. Fu, X.M. Lai, Size effect affected formability of sheet metals in micro/meso scale plastic deformation: Experiment and modeling, International Journal of Plasticity, 68 (2015) 34-54. https://doi.org/10.1016/j.ijplas.2014.11.002.
[43] X.F. Tang, L.F. Peng, S.Q. Shi, M.W. Fu, Influence of crystal structure on size dependent deformation behavior and strain heterogeneity in micro-scale deformation, International Journal of Plasticity, 118 (2019) 147-172. https://doi.org/10.1016/j.ijplas.2019.02.004.
[44] F. Barlat, J.J. Gracio, M.-G. Lee, E.F. Rauch, G. Vincze, An alternative to kinematic hardening in classical plasticity, International Journal of Plasticity, 27 (2011) 1309-1327. https://doi.org/10.1016/j.ijplas.2011.03.003.
[45] J. Lee, D. Kim, Y.S. Lee, H.J. Bong, F. Barlat, M.G. Lee, Stress update algorithm for enhanced homogeneous anisotropic hardening model, Computer Methods in Applied Mechanics and Engineering, 286 (2015) 63-86. https://doi.org/10.1016/j.cma.2014.12.016.
[46] F. Barlat, J.J. Ha, J.J. Grácio, M.G. Lee, E.F. Rauch, G. Vincze, Extension of

homogeneous anisotropic hardening model to cross-loading with latent effects, International Journal of Plasticity, 46 (2013) 130-142. https://doi.org/10.1016/j.ijplas.2012.07.002.
[47] J.Q. Ran, M.W. Fu, W.L. Chan, The influence of size effect on the ductile fracture in micro-scaled plastic deformation, International Journal of Plasticity, 41 (2013) 65-81. https://doi.org/10.1016/j.ijplas.2012.09.002.
[48] V.I. Yamakov, D.H. Warner, R.J. Zamora, E. Saether, W.A. Curtin, E.H. Glaessgen, Investigation of crack tip dislocation emission in aluminum using multiscale molecular dynamics simulation and continuum modeling, Journal of the Mechanics and Physics of Solids, 65 (2014) 35-53. https://doi.org/10.1016/j.jmps.2013.12.009.
[49] W. Zhou, J. Yu, J. Lin, T.A. Dean, Manufacturing a curved profile with fine grains and high strength by differential velocity sideways extrusion, International Journal of Machine Tools and Manufacture, 140 (2019) 77-88. https://doi.org/10.1016/j.ijmachtools.2019.03.002.
[50] E.O. Hall, The Deformation and Ageing of Mild Steel: III Discussion of Results, Proceedings of the Physical Society. Section B, 64 (1951) 747-753. https://doi.org/10.1088/0370-1301/64/9/303.
[51] N.J. Petch, The cleavage strength of polycrystals, Journal of the Iron and Steel Institute, 174 (1953) 25-28.
[52] H. Mecking, U.F. Kocks, Kinetics of flow and strain-hardening, Acta Metallurgica, 29 (1981) 1865-1875. https://doi.org/10.1016/0001-6160(81)90112-7.
[53] J.H. Schmitt, E. Aernoudt, B. Baudelet, Yield loci for polycrystalline metals without texture, Materials Science and Engineering, 75 (1985) 13-20. https://doi.org/10.1016/0025-5416(85)90173-9.